

Supplemental Material for “Unmasking the Origin of Kinks in the Photoemission Spectra of Cuprate Superconductors”

Zhenglu Li, Meng Wu, Yang-Hao Chan, and Steven G. Louie*

Department of Physics, University of California at Berkeley, Berkeley, CA 94720, USA and Materials Sciences Division, Lawrence Berkeley National Laboratory, Berkeley, CA 94720, USA.

*Email: sglouie@berkeley.edu

I. Computational details

This work involves three major computation steps: 1) DFPT calculation using the ABINIT code [29]; 2) *GWPT* calculation using the BerkeleyGW code [19,20,30,31]; and 3) Wannier interpolation using the EPW code [32,59]. We have developed wrappers to link the three codes.

We perform DFT and DFPT calculations of $\text{La}_{2-x}\text{Sr}_x\text{CuO}_4$ (LSCO) using the ABINIT code [29]. The Sr doping effect of $x = 0.15$ and $x = 0.30$ is simulated by removing electrons from the crystal and adding a compensating negative charge background [5]. We use norm-conserving pseudopotentials [33,34] with generalized gradient approximation to the exchange-correlation functional [35], and a plane-wave basis with a cutoff set to 100 Ry. At each doping, the structures are fully optimized by minimizing the forces on each of the 7 atoms in the primitive cell of the tetragonal crystal structure (the primitive cell lattice vectors are $\mathbf{a}_1 = (0, \frac{a}{\sqrt{2}}, -\frac{c}{2})$, $\mathbf{a}_2 = (0, -\frac{a}{\sqrt{2}}, -\frac{c}{2})$, $\mathbf{a}_3 = (-\frac{a}{\sqrt{2}}, 0, \frac{c}{2})$; at $x = 0.15$, the optimized $a = 3.777$ Å and $c = 13.106$ Å; at $x = 0.30$, the optimized $a = 3.750$ Å and $c = 12.981$ Å), followed by DFT (\mathbf{k} grid set to $32 \times 32 \times 32$) and DFPT (\mathbf{k} grid set to $8 \times 8 \times 8$ and \mathbf{q} grid set to $4 \times 4 \times 4$) calculations for the ground-state properties and the linear-response changes due to atom displacements (21 patterns) at each \mathbf{q} , respectively.

The *GWPT* calculation is performed with a screened Coulomb interaction cutoff of 25 Ry and a bare Coulomb interaction cutoff of 100 Ry using the BerkeleyGW code [20,30,31]. The inverse dielectric matrix $\epsilon_{\mathbf{G}\mathbf{G}'}^{-1}(\mathbf{p})$ (where \mathbf{G} 's are the reciprocal lattice vectors) and the linear-response changes in the self-energy $\partial_{\mathbf{q}\nu} \Sigma^{e-e}(\mathbf{r}, \mathbf{r}'; \epsilon)$ are constructed with 200 bands and $8 \times 8 \times 8$ internal \mathbf{p} grid [20].

The *e-ph* matrix elements $g_{mn\nu}^{\text{DFT}}(\mathbf{k}, \mathbf{q})$ and $g_{mn\nu}^{\text{GW}}(\mathbf{k}, \mathbf{q})$ from DFPT and *GWPT*, respectively, are directly computed on coarse $4 \times 4 \times 4$ \mathbf{k} and \mathbf{q} grids, and then interpolated with a Wannier function approach [36,37] using the EPW code [32]. The gauge of the wavefunctions and matrix elements must be handled consistently through the whole procedure (i.e., in DFPT, *GWPT*, and Wannier interpolation). The Wannier subspace includes 17 Wannier orbitals corresponding to the five *d* orbitals of the Cu atom and three *p* orbitals of each of the four O atoms. To compute the phonon-induced electron self-energy $\Sigma_{n\mathbf{k}}^{e-p}$, 1,000,000 random phonon \mathbf{q} points are sampled along with a 2 meV smearing factor. For the calculation of the *e-ph* coupling constant λ , interpolated $32 \times 32 \times 32$ \mathbf{k} and $16 \times 16 \times 16$ \mathbf{q} grids are used. Note that the computation of $\Sigma_{n\mathbf{k}}^{e-ph}$ requires a much denser sampling to resolve the fine energy-dependent features within the phonon frequency range, whereas λ is an averaged quantity on the Fermi surface and therefore converges relatively faster. Other convergence parameters are consistent with the previous DFPT-level study [5] and are tested by ourselves to produce converged results.

The DFPT calculations directly compute all the *e-ph* matrix elements (full *m*, *n*, *v*, \mathbf{k} , and \mathbf{q} dependence) within the Cu-O manifolds. However, because of the extremely expensive computational resource required by *GWPT* calculations, we compute a subset of *GWPT* matrix elements that gives the most dominant contributions. The *GWPT* calculations directly compute (for all phonon $\mathbf{q}\nu$ modes): 1) the matrix elements within the single band crossing E_F among all \mathbf{k} and \mathbf{q} points, and 2) the matrix elements

from the single coarse-grid \mathbf{k} point on the band crossing E_F (the electron state closest to the nodal kink on the coarse grid) to all the other 16 Cu-O bands via all \mathbf{q} points. The less important matrix elements are replaced by their DFPT values in the following Wannier interpolation calculations. We have checked that this subset of explicitly computed $GWPT$ e -ph matrix elements accounts for the overwhelming majority of the correlation enhancement effect and produces the main physics of the photoemission kink. Our procedure in fact places a lower bound on the correlation enhancement of the e -ph coupling.

Note that soft phonon modes may arise from direct $T = 0$ K DFPT calculations because we are forcing a tetragonal primitive unit cell whereas in reality structural distortions set in at low temperature [5]. We have thus adopted a common phonon stabilization procedure using high-temperature sampled structures to proceed with the e -ph coupling calculations [20,38,39]. We perform *ab initio* molecular dynamics calculations with $2 \times 2 \times 2$ supercells at 300 K using the VASP code [40] with projected augmented wave pseudopotentials [41]. After thermal equilibrium is reached, 50 randomly sampled structures are picked with their forces being fitted to harmonic potentials using the ALAMODE code [42]. The dynamical matrices are constructed using the fitted harmonic potentials and then later read by EPW for interpolations.

II. Theoretical formalism

The core quantity for building microscopic e -ph theories is the e -ph matrix element $g_{mnv}(\mathbf{k}, \mathbf{q})$ that measures the coupling amplitude of a quasiparticle from the initial quasiparticle state $|\psi_{n\mathbf{k}}\rangle$ to a final state $|\psi_{m\mathbf{k}+\mathbf{q}}\rangle$ via a phonon mode labeled by \mathbf{qv} . Such a process can be directly and efficiently calculated using first principles in the primitive unit cell by taking advantage of linear-response theory. Within $GWPT$, the e -ph matrix elements at the GW level are constructed as [20],

$$g_{mnv}^{GW}(\mathbf{k}, \mathbf{q}) = \langle \psi_{n\mathbf{k}} | \partial_{\mathbf{qv}} V_{\text{ion}} + \partial_{\mathbf{qv}} V_H | \psi_{m\mathbf{k}+\mathbf{q}} \rangle + \langle \psi_{n\mathbf{k}} | \partial_{\mathbf{qv}} \Sigma^{e-e}(\mathbf{r}, \mathbf{r}'; \varepsilon) | \psi_{m\mathbf{k}+\mathbf{q}} \rangle, \quad (\text{S1})$$

where V_{ion} is the ionic potential seen by the electrons, V_H is the Hartree potential, and $\Sigma^{e-e}(\mathbf{r}, \mathbf{r}'; \varepsilon)$ is the electron self-energy operator that contains the electron-electron interaction effects. The e -ph matrix element at the DFT level $g_{mnv}^{\text{DFT}}(\mathbf{k}, \mathbf{q})$ is calculated using DFPT in which $\partial_{\mathbf{qv}} \Sigma^{e-e}(\mathbf{r}, \mathbf{r}'; \varepsilon)$ is simply approximated as the change in the static exchange-correlation potential $\partial_{\mathbf{qv}} V_{\text{xc}}(\mathbf{r})$. The resulting matrix elements in fact only describe the interaction of the fictitious independent Kohn-Sham particles with the phonons. A calculation of the linear-response change in Σ^{e-e} due to phonons using $GWPT$ captures physically the many-electron self-energy effects in the interaction of a true quasiparticle with phonons (i.e., the true e -ph matrix element $g_{mnv}^{GW}(\mathbf{k}, \mathbf{q})$), hence providing more accurate descriptions of the e -ph interactions. The change in the GW self-energy is [20],

$$\partial_{\mathbf{qv}} \Sigma^{e-e}(\mathbf{r}, \mathbf{r}'; \varepsilon) = i \int \frac{d\varepsilon'}{2\pi} e^{-i\delta\varepsilon'} \partial_{\mathbf{qv}} G(\mathbf{r}, \mathbf{r}'; \varepsilon - \varepsilon') W(\mathbf{r}, \mathbf{r}'; \varepsilon'), \quad (\text{S2})$$

where $\delta = 0^+$, $G(\mathbf{r}, \mathbf{r}'; \varepsilon - \varepsilon')$ is the single-particle Green's function, and $W(\mathbf{r}, \mathbf{r}'; \varepsilon')$ is the screened Coulomb interaction. In Eq. (S2), we neglected the change in W due to phonons by adopting the constant-screening approximation [20,43], which is equivalent to the well-justified approximation $\frac{\delta W}{\delta G} \approx 0$ used in the *ab initio* GW plus Bethe-Salpeter equation (GW -BSE) formalism for exciton physics [44–46].

The e -ph interaction contribution to the electron self-energy $\Sigma^{e\text{-ph}}$ can then be constructed at either the $GWPT$ level (using $g_{mnv}^{GW}(\mathbf{k}, \mathbf{q})$) or at the DFPT level (using $g_{mnv}^{\text{DFT}}(\mathbf{k}, \mathbf{q})$) within the Fan-Migdal approximation as [17,60–62,32],

$$\Sigma_{n\mathbf{k}}^{e\text{-ph}}(\omega) = \sum_{\mathbf{q}} \sum_m |g_{mnv}(\mathbf{k}, \mathbf{q})|^2 \times \left[\frac{f_{m\mathbf{k}+\mathbf{q}} + n_{\mathbf{qv}}}{\omega - \varepsilon_{m\mathbf{k}+\mathbf{q}} + \omega_{\mathbf{qv}} + i\delta} + \frac{1 - f_{m\mathbf{k}+\mathbf{q}} + n_{\mathbf{qv}}}{\omega - \varepsilon_{m\mathbf{k}+\mathbf{q}} - \omega_{\mathbf{qv}} + i\delta} \right], \quad (\text{S3})$$

where $f_{n\mathbf{k}}(T)$ is the Fermion occupation number and $n_{\mathbf{q}\nu}(T)$ is the Boson occupation number, $\varepsilon_{n\mathbf{k}}$ is the DFT eigenvalue, and $\omega_{\mathbf{q}\nu}$ is the phonon frequency. Self-consistently using GW eigenvalues, which undergo band reordering from the DFT results within the Cu-O bands, for Eq. (S3) is technically challenging when combined with Wannier interpolation. However, this may be avoided since the effect from GW correction in the band structure (via Fermi velocity and band width) to Eq. (S3) is estimated to be one order of magnitude smaller than the effect from the GW renormalization in the e -ph coupling strength. The first (second) term in the bracket corresponds to phonon emission (absorption) processes. At low temperature, the phonon emission process dominates $\Sigma^{e-\text{ph}}$ and hence the phonon-induced kink in the photoemission spectrum. $\text{Re}\Sigma_{n\mathbf{k}}^{e-\text{ph}}(E_F)$ is subtracted from the computed $\Sigma_{n\mathbf{k}}^{e-\text{ph}}(\omega)$ to impose the sum rule of electron number conservation (Luttinger theorem) such that $\text{Re}\bar{\Sigma}_{n\mathbf{k}}^{e-\text{ph}}(\omega) = \text{Re}\Sigma_{n\mathbf{k}}^{e-\text{ph}}(\omega) - \text{Re}\Sigma_{n\mathbf{k}}^{e-\text{ph}}(E_F)$ is zero at E_F [17,32]. Note that $\text{Re}\Sigma_{n\mathbf{k}}^{e-\text{ph}}(E_F)$ remains nearly constant at different \mathbf{k} for the system studied in this work, therefore imposing the sum rule is basically equivalent to redefining E_F (with a rigid shift) for the quasiparticle excitations. The electron spectral function including interaction with phonons is constructed from the calculated phonon-induced part of the self-energy as [17,32],

$$A_{n\mathbf{k}}(\omega) = \frac{1}{\pi} \frac{|\text{Im}\Sigma_{n\mathbf{k}}^{e-\text{ph}}(\omega)|}{\left|\omega - \varepsilon_{n\mathbf{k}} - \text{Re}\bar{\Sigma}_{n\mathbf{k}}^{e-\text{ph}}(\omega)\right|^2 + \left|\text{Im}\Sigma_{n\mathbf{k}}^{e-\text{ph}}(\omega)\right|^2}, \quad (\text{S4})$$

and the Fermi factor $f_{n\mathbf{k}}(T)$ is imposed in plotting the intensity map [67] of Figs. 2(a) and 2(c) in the main text.

III. Low-energy behavior of phonon-induced part of self-energy

Figure 1 in the main text shows a rapid variation in $\text{Re}\bar{\Sigma}_{n\mathbf{k}}^{e-\text{ph}}$ and $\text{Im}\Sigma_{n\mathbf{k}}^{e-\text{ph}}$ mainly occurs for electronic states between E_F and a binding energy corresponding to the maximum phonon frequency $\omega_{\text{ph}}^{\text{max}} \sim 87$ meV in LSCO. It is well-understood within the e -ph mechanism. At low temperature, a quasi-hole state $n\mathbf{k}$ excited below E_F can scatter to other hole states via emitting a phonon, and two resonant scattering regimes (along with non-resonant scatterings) contribute to $\Sigma_{n\mathbf{k}}^{e-\text{ph}}(E_{n\mathbf{k}})$: 1) If the hole excitation energy (given by $E_F - E_{n\mathbf{k}}$) is within the range of all possible phonon frequencies, i.e. $E_F - E_{n\mathbf{k}} < \omega_{\text{ph}}^{\text{max}}$, the final hole states must have a yet still positive but lower excitation energy (i.e. smaller binding energy in ARPES) than $E_F - E_{n\mathbf{k}}$ (energy conservation via emitting a phonon), restricting some phonon modes from participating. Therefore, $\Sigma_{n\mathbf{k}}^{e-\text{ph}}(E_{n\mathbf{k}})$ is expected to be finely structured through phonon-mode dependent coupling strength as well as the phonon DOS. 2) In contrast, if $E_F - E_{n\mathbf{k}} > \omega_{\text{ph}}^{\text{max}}$, all phonon channels are available for emission, and thus the scattering process is dominated by the final hole DOS, making $\Sigma_{n\mathbf{k}}^{e-\text{ph}}(E_{n\mathbf{k}})$ a smoother function of energy [5]. The resonant channels uniquely determine the scattering rates reflected in $\text{Im}\Sigma_{n\mathbf{k}}^{e-\text{ph}}$, whereas $\text{Re}\bar{\Sigma}_{n\mathbf{k}}^{e-\text{ph}}$ has contributions from both resonant and non-resonant processes.

In a simple Holstein model where a single electron band couples to an Einstein phonon mode, the peak of the $\text{Re}\bar{\Sigma}_{n\mathbf{k}}^{e-\text{ph}}$ is determined by a single uniform e -ph coupling parameter $|g|$. However, in complex materials (such as LSCO in this work), the e -ph mode-coupling strength reflected in $\text{Re}\bar{\Sigma}_{n\mathbf{k}}^{e-\text{ph}}$ at a particular phonon mode frequency involves contributions from all other electronic states [see Eq. (S3)].

IV. Extraction of kinks from spectral functions

The procedure for the extraction of the size and position of the photoemission kinks is described in the main text, following the common experimental practice. We note that the DFT band structure [Fig. 4(c) in the main text] within the energy range of interest (along the nodal direction) is well represented as a linear dispersion relation $\varepsilon_{n\mathbf{k}} = \hbar\mathbf{v}_0 \cdot (\mathbf{k} - \mathbf{k}_F)$ where \mathbf{v}_0 is the DFT Fermi velocity (note that E_F is set to zero here). The quasiparticle energy due to e -ph interaction at a given temperature is,

$$E_{n\mathbf{k}} = \varepsilon_{n\mathbf{k}} + \text{Re}\bar{\Sigma}_{n\mathbf{k}}^{e-\text{ph}}(E_{n\mathbf{k}}). \quad (\text{S5})$$

Since the reference line is determined by the two points at \mathbf{k}_F and \mathbf{k}_1 on the dispersion relation along the nodal direction, we can write the expression of this reference line [black dashed lines in Figs. 2(e) and 2(f) in the main text] as,

$$e_{n\mathbf{k}} = E_1 \times \frac{|\mathbf{k} - \mathbf{k}_F|}{|\mathbf{k}_1 - \mathbf{k}_F|}. \quad (\text{S6})$$

The kink is extracted as the deviation of $E_{n\mathbf{k}}$ from $e_{n\mathbf{k}}$ at each \mathbf{k} , i.e., $\text{kink}(E_{n\mathbf{k}}) = E_{n\mathbf{k}} - e_{n\mathbf{k}}$, and by using the linearity of $\varepsilon_{n\mathbf{k}}$, it becomes,

$$\text{kink}(E_{n\mathbf{k}}) = \text{Re}\bar{\Sigma}_{n\mathbf{k}}^{e-\text{ph}}(E_{n\mathbf{k}}) - \text{Re}\bar{\Sigma}_{n\mathbf{k}_1}^{e-\text{ph}}(E_1) \times \frac{|\mathbf{k} - \mathbf{k}_F|}{|\mathbf{k}_1 - \mathbf{k}_F|}, \quad \text{with } E_{n\mathbf{k}} \in [E_F, E_1]. \quad (\text{S7})$$

Eq. (S7) is true in the quasiparticle limit ($\text{Im}\Sigma \ll \text{band width}$). Moreover, when $\text{Re}\bar{\Sigma}_{n\mathbf{k}}^{e-\text{ph}}$ (which is 20–30 meV in peak value) is comparatively small to the electron band energy range of interest (100–200 meV in this work), the kink strength can be *approximately* expressed as,

$$\text{kink}(E_{n\mathbf{k}}) \approx \text{Re}\bar{\Sigma}_{n\mathbf{k}}^{e-\text{ph}}(E_{n\mathbf{k}}) - \text{Re}\bar{\Sigma}_{n\mathbf{k}_1}^{e-\text{ph}}(E_1) \times \frac{E_{n\mathbf{k}}}{E_1}. \quad (\text{S8})$$

Eq. (S8) means that one can draw a straight reference line connecting the two points, $(E_F, \text{Re}\bar{\Sigma}_{n\mathbf{k}_F}^{e-\text{ph}}(E_F))$ (i.e. the origin) and $(E_1, \text{Re}\bar{\Sigma}_{n\mathbf{k}_1}^{e-\text{ph}}(E_1))$ on the $\text{Re}\bar{\Sigma}_{n\mathbf{k}}^{e-\text{ph}}$ -vs.- $E_{n\mathbf{k}}$ curve, and the kink size can be *approximated* as the difference between $\text{Re}\bar{\Sigma}_{n\mathbf{k}}^{e-\text{ph}}(E_{n\mathbf{k}})$ and this reference line at each $E_{n\mathbf{k}}$.

To extract the experimental kink data, we fit linearly data points with binding energy between 0 and 30 meV to determine \mathbf{k}_F . We fit linearly data points *available* (not all experiments considered span this full range) between 100 and 200 meV binding energies and use $E_1 = -0.12$ eV in the fitted dispersion relation to determine \mathbf{k}_1 . Then we use the two points (\mathbf{k}_F, E_F) and (\mathbf{k}_1, E_1) to determine the reference bare-band line for the extraction of the kink deviation. The extracted kink data are consistent among different experiments [3,21,23–26], thus providing confident quantitative comparisons with theory.

The experimental MDC width is in general composed of several contributions, including impurity scattering (presumably relatively constant with respect to energy), electron-electron interaction (power law behavior as a function of binding energy), and e -ph interaction (saturates at energies beyond $\omega_{\text{ph}}^{\text{max}}$) [68]. Following standard practice by experimental groups, we extract the experimental e -ph MDC width plotted in Figs. 2(g) and 2(h), by first fitting a power law function to the original measured MDC FWHM data [22] between the binding energy of 100 and 200 meV for electron-electron contribution, and then subtracting off this fitted function and the impurity contribution (taken to be the width at E_F) from the original data in the whole range. The data points after subtraction are denoted as experimental MDC FWHM width from e -ph coupling and are plotted in Figs. 2(g) and 2(h) in the main text. Note that large uncertainty exists in the e -ph MDC width extraction, depending on the choice of fitting range, and therefore the comparisons in Figs. 2(g) and 2(h) are qualitative.

In some early experiments [21,22], the heavily overdoped ($x = 0.30$) data show unsatisfactory statistics and the extracted quantity does not qualitatively agree with more recent data [23]. Therefore, we have not used those $x = 0.30$ experimental data in comparisons with theory in Figs. 2–4 in the main text.

V. Electron-phonon coupling constant λ

We calculate the e -ph coupling constant λ on the Fermi surface [17,60–62], although phonons alone are not expected to be responsible for the d -wave superconductivity in single-layer cuprates [68]. Our $GWPT$ calculation gives $\lambda = 0.55$ for $x = 0.15$, and $\lambda = 0.54$ for $x = 0.30$ (whereas DFPT gives $\lambda = 0.26$ for $x = 0.15$ and $\lambda = 0.27$ for $x = 0.30$, consistent with previous DFPT studies [5,6]), evidencing a moderately strong e -ph coupling constant in LSCO.

VI. $GWPT$ validation set of metals

To demonstrate the validity of the $GWPT$ method and to highlight correlation-enhancement in the e -ph coupling in LSCO (and also in $\text{Ba}_{1-x}\text{K}_x\text{BiO}_3$ (BKBO) [20]), we performed a series of $GWPT$ calculations of the e -ph coupling constant λ on five conventional metals: 1) Cu, 2) Al, 3) In, 4) ZrN, and 5) Nb. This set of materials covers a non-superconductor, as well as weakly-, moderately- and strongly-coupled phonon-driven superconductors. For this validation set, the e -ph matrix elements at both DFPT and $GWPT$ levels are computed on $8 \times 8 \times 8$ \mathbf{k} and $4 \times 4 \times 4$ \mathbf{q} grids which are then interpolated to finer grids by Wannier functions [32,36,37,59]. The DFPT calculations use a 60 Ry plane-wave cutoff. The $GWPT$ calculations use a 15 Ry plane-wave cutoff and an $8 \times 8 \times 8$ \mathbf{p} grid for the screened Coulomb interaction, and a total of 200 bands for band summations. A dense Brillouin zone wavevector sampling may be needed for complicated Fermi surfaces composed of multiple bands with disconnected small pockets, such as in Al. The Wannierization processes [32,59] interpolate the e -ph matrix elements to finer $40 \times 40 \times 40$ \mathbf{k} and $20 \times 20 \times 20$ \mathbf{q} grids for the e -ph coupling calculations. Here we list the *initial* Wannier projections used for each material: 1) Cu: 3d, 4s, 4p; 2) Al: 3s, 3p, 3d; 3) In: 5s, 5p; 4) ZrN: 4s, 4p, 4d, 5s, 5p for Zr, and 2s, 2p for N; and 5) Nb: 4d, 5s, 5p. The e -ph coupling constant λ is computed at both DFPT and $GWPT$ levels, and are plotted in Fig. S3 together with results of BKBO from an earlier work [20]. The corresponding measured λ from tunneling experiments [47–53] are included for comparison.

In this validation set, our DFPT results are consistent with other earlier DFPT calculations [54–57]. Given the experimental uncertainties (which may be up to few tens of percent, see discussions in, e.g. Ref. [58]) and the numerical uncertainties, we consider the overall agreement between the values for λ from $GWPT$ and experiments is good (maximum difference in λ is ~ 0.1 for the five conventional metals). In the oxide BKBO, λ is significantly enhanced by over a factor of 2 in $GWPT$ (due to many-electron correlations) compared with DFPT (see Fig. S3 and Ref. [20]). Around the optimal doping of BKBO, the tunneling experiment extracted $\lambda^{\text{expt.}} = 1.2$ [53] and our previous $GWPT$ results give $\lambda^{GWPT} = 1.14$ agreeing with the experiment, whereas DFPT fails significantly giving $\lambda^{\text{DFPT}} = 0.47$ [20]. This $GWPT$ validation set on five conventional metals as well as an oxide metal establishes $GWPT$ as a reliable method to study e -ph interaction and its use in exploring the intriguing interplay between many-electron correlations and e -ph interactions in more “unconventional” materials.

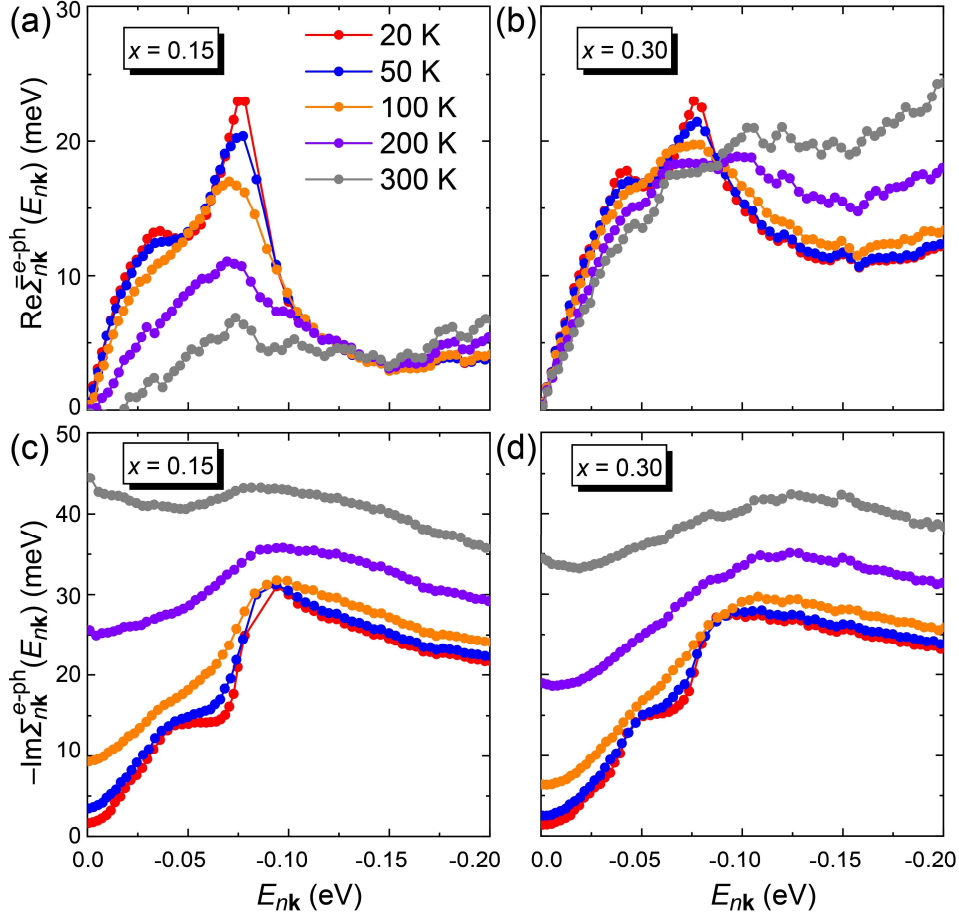


FIG. S1. (a),(b) Temperature dependence of $\text{Re}\bar{\Sigma}_{nk}^{e-ph}(E_{nk})$ of LSCO at (a) $x = 0.15$ and (b) $x = 0.30$ from *GWPT* calculations. In the optimally doped case ($x = 0.15$), increasing temperature reduces the $\text{Re}\bar{\Sigma}_{nk}^{e-ph}(E_{nk})$ peak height, whereas in the overdoped case ($x = 0.30$), the high binding energy (> 0.1 eV) tail rises with increasing temperature. This is due to a closer proximity of the states to the higher density features of the DOS distribution in the overdoped case. (c),(d) Temperature dependence of $\text{Im}\Sigma_{nk}^{e-ph}(E_{nk})$ of LSCO at (c) $x = 0.15$ and (d) $x = 0.30$. The effects of high temperatures in both $\text{Re}\bar{\Sigma}_{nk}^{e-ph}$ and $\text{Im}\Sigma_{nk}^{e-ph}$ blur the kink feature and broaden the spectral functions.

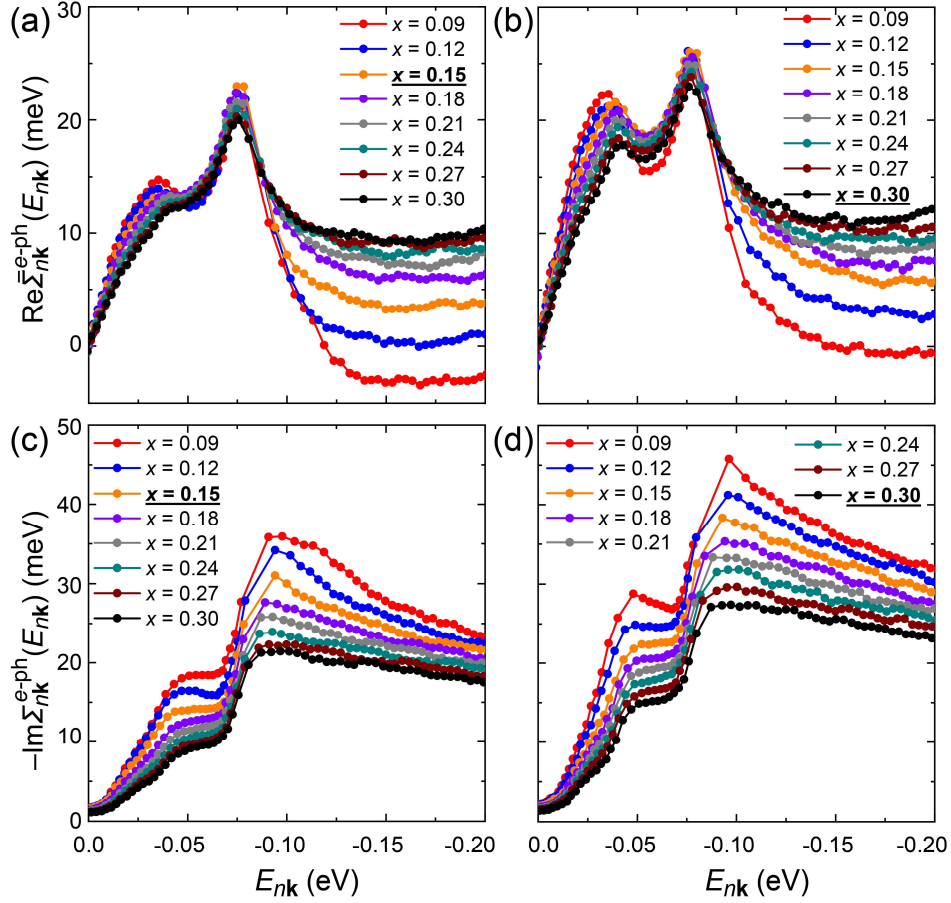


FIG. S2. (a),(b) Doping dependence of $\text{Re}\bar{\Sigma}_{nk}^{e-ph}(E_{nk})$ (at *GWPT* level) constructed within rigid-band approximation using the *e-ph* matrix elements directly calculated at $x = 0.15$ and $x = 0.30$ (indicated by underline), given respectively by panels (a) and (b). A significant elevation of the high binding energy tail (> 0.1 eV) in the $\text{Re}\bar{\Sigma}_{nk}^{e-ph}(E_{nk})$ with increasing hole doping is observed, due to the sharp multi-band features in the electron DOS. The main peak height of $\text{Re}\bar{\Sigma}_{nk}^{e-ph}(E_{nk})$ shows only slight changes. (c),(d) Doping dependence of $\text{Im}\bar{\Sigma}_{nk}^{e-ph}(E_{nk})$ (at *GWPT* level) constructed within rigid-band approximation using the *e-ph* matrix elements directly calculated at $x = 0.15$ and $x = 0.30$ (indicated by underline), given respectively in panels (c) and (d).

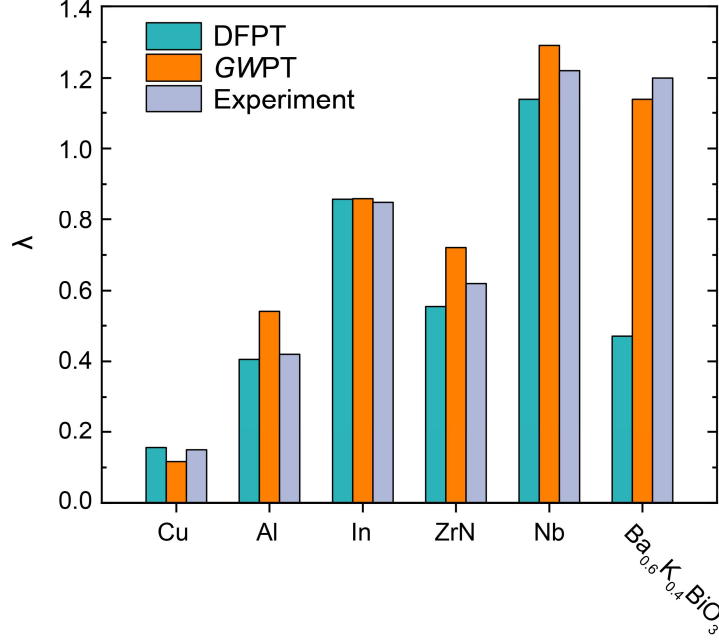


FIG. S3. DFPT- and $GWPT$ -computed e -ph coupling constant λ for a validation set of sp -band conventional metals (Cu, Al, In) and d -band conventional metals (ZrN, Nb), along with the oxide metal BKBO [20]. Experimental values are taken from tunneling experiments [47] for Cu [48], Al [49], In [50], ZrN [51], Nb [52], and BKBO [53], respectively. For the conventional metals studied here, DFPT and $GWPT$ both agree with experiments within the experimental and numerical uncertainties. For materials with strong correlations, e.g. BKBO, DFPT fails significantly whereas $GWPT$ successfully capture the many-electron effects in the measured λ [20].